



2018 Volume:18 Pages:17-31

Structural and Magnetic Properties of Second Row Transition Metal Doped Iron Oxide Nanoparticles

Santosh Kumar

Department of Physics,
College of Commerce, Arts and Science, Patna-800020
Email id: skphysics@yahoo.co.in

ABSTRACT

Magnetic Nanoparticles of Fe_3O_4 doped by different amounts of Y^{3+} (0, 0.1, 1 and 10%) have been synthesized by chemical route. Single phase formation has been confirmed by X-Ray diffraction measurement. An improved magnetisation has been observed in SQUID-VSM measurement for the Fe_3O_4 sample with 1% Y^{3+} doping. The surface morphology and particle size distribution have been confirmed by SEM and TEM measurements. The results obtained are suggestive of the suitability of Y^{3+} doped Fe_3O_4 Nanoparticles for biomedical applications specially for hyperthermia treatment.

Keywords : Spinel Ferrite, Ferromagnetism, Double Exchange Interaction,

Paper History: Paper Received on 30/11/2017, Accepted on 14/02/2018 Published on 15/03/2018



INTRODUCTION

Magnetic iron oxide nanoparticles (NPs) have fascinated researchers and have attracted their attention due to their exceptional magnetic properties showing great potential in bio-related applications. The most commonly studied magnetic iron oxides are hematite (α - Fe_2O_3 : rhombohedral crystal structure), maghemite (γ - Fe_2O_3 : cubic), and magnetite (Fe_3O_4), which is isostructural with γ - Fe_2O_3 with one important feature depending on iron cations having two different valence states (Fe^{2+} and Fe^{3+} in the ratio of 1:2). Fe_3O_4 belongs to the spinel ferrite family with a general chemical formula of AB_2O_4 and crystallizes in a cubic system ($Fd\bar{3}m$ space group). However, there is a probability of complete transformation of Fe^{2+} oxidation into Fe^{3+} resulting into a chemical transformation of Fe_3O_4 (FeFe_2O_4) into γ - Fe_2O_3 or even α - Fe_2O_3 ¹. Unfortunately, the oxidation step between Fe_3O_4 and γ - Fe_2O_3 is hard to be detected by the X-ray powder diffraction technique because their diffraction patterns are almost similar and the sample color also does not differ much (dark brown or even black). However, It is much easier to recognize the transformation of Fe_3O_4 into α - Fe_2O_3 since the latter crystallizes in a rhombohedral system ($R\bar{3}c$) giving a totally different diffraction pattern and there is a significant change in sample color also (from dark black brown into red). The importance of this critical issue has several consequences:

1. change in the magnetic behavior, which is critical in view of its potential bio-related applications
2. an oxidation process which leads to the well-known Fenton reaction, creation of the reactive oxide species (ROS) and programmed cell death and
3. lack of chemical stability of the material itself, which can be detrimental to the engineered material properties (efficacy of the heat induction).

It is known from the previous studies that ferrite NPs have already attracted considerable attention due to their interesting magnetic properties and high prospect in biomedical applications such as magnetic drug delivery, magnetic resonance imaging, magnetic separation, or hyperthermia.²⁻⁶ In spite of the issues described above, magnetite NPs are used in cancer diagnostics and therapy^{3,7} and were also approved by the Food and Drug Administration (FDA) as contrast agents in magnetic resonance. Moreover, the second and third phases of clinical research using Fe_3O_4 NPs in hyperthermia as cancer therapy have already been carried out in Germany without any noticeable toxic effects⁸.

Fe_3O_4 crystallizes in an inverse spinel structure. Large Oxygen ions are tightly packed in a cubic order, while smaller Fe^{3+} ions fill completely the eight sites of the tetrahedral subnetwork. The octahedral positions are occupied by Fe^{2+} and Fe^{3+} ions. Because the magnetic spins of the tetra- and octahedral networks are arranged in the



opposite direction, the structure is ferrimagnetic⁹. Magnetic properties of magnetite owes its origin from the separation of 5d orbitals. Orbitals are divided into subgroups due to the presence of a field of ligands which is oxide in this case. This implies that the Fe³⁺ and Fe²⁺ ions have one pair of paired electrons and four unpaired electrons. In octahedral coordination (where the d sub shell divides into two subgroups E_g and T_{2g}), iron ions are ferromagnetically coupled via the so-called double exchange mechanism. One of the electrons from a paired pair can be exchanged between two octahedral coordinates. In contrast, Fe³⁺ ions in tetra- and octahedral sites are coupled antiferromagnetically by an oxygen atom, which means that Fe³⁺ spins add with each other to zero. Hence, only unpaired Fe²⁺ spins in an octahedral coordination contribute to magnetization¹⁰.

The Fe²⁺ ions in Fe₃O₄ can be replaced with another divalent transition metal M²⁺ (for example, M = Zn, Mn, Ni, Co, Cu, etc.), to obtain a MFe₂O₄ ferrite crystal in an inverted spinel structure. The magnetization depends mainly on unpaired d electrons from M²⁺. However, when M²⁺ is small enough, MFe₂O₄ can adopt a spinel structure in which two Fe³⁺ occupy octahedral sites, and M²⁺ occupies tetrahedral sites, and there is no anti-ferromagnetic coupling between the two Fe³⁺ ions. This structure provides a higher magnetization value than that of the reverse spinel structure of MFe₂O₄¹¹⁻¹⁶.

Iron ion nanoparticles doped with metal ions, such as CoFe₂O₄, NiFe₂O₄, and MnFe₂O₄, show strong magnetic properties as well as an improved contrast effects in magnetic resonance imaging (MRI), which are much better than those of conventional Fe₃O₄ NPs¹⁷. Nevertheless, the use of these M²⁺ doped iron oxide nanoparticles in biomedical research is severely hampered by the high levels of toxicity present due to the presence of these transition metals (Co, Ni, and Mn)¹⁸⁻²⁰. Zn ions are one of the widely studied dopants in iron oxide nanoparticles, which have a high magnetization value which significantly enhances their MRI contrast and hyperthermic effects. Their initial in vitro and in vivo studies showed that Zn²⁺ doped Fe₃O₄ is non-toxic and potentially useful in biology and medicine^{21,22}.

Another dopant used to improve the magnetic properties of Fe₃O₄ are lanthanide ions (Ln³⁺). Lanthanide ions as dopants are interesting due to the unique optical and magnetic properties associated with their f electron configurations^{23,24}. Magnetite doping can change its magnetic, dielectric, and structural properties by adding, e.g., trivalent cations such as Nd³⁺, Cr³⁺, Y³⁺, or In³⁺. Rare-earth cations such as La³⁺, Sm³⁺, or Dy³⁺, by substituting Fe³⁺ in the octahedral position, release iron ions to coordinate in the tetrahedral position, which alleviates the lattice tension. Due to this, the amount and type of Ln³⁺ doping changes the magnetisation, permeability and electrical resistance of magnetite²⁵⁻³². Milanović et al²⁵ observed decreasing saturation magnetization after In³⁺



ion doping of ZnFe_2O_4 , but after Y^{3+} ion doping, they observed increasing magnetization compared with undoped NPs but only for small amount of dopants (0.15%). They suggest that Y^{3+} ions stabilize Fe^{3+} ions in the octahedral sites which reduces the tendency toward inversion²⁵.

In the present work, Fe_3O_4 NPs have been doped with yttrium ions to increase the magnetization of the material for its probable use in magnetic hyperthermia treatment. The addition of yttrium ions reaches their maximum in the range from 1 to 1.5 mol % (relative to moles of Fe^{3+}). With a further increase of the dopant, the second nanocrystalline phase precipitates. For now, the Fe_3O_4 NP doping by Y^{3+} ions has not been investigated for a magnetic increase and hyperthermia application.

Hyperthermia is a therapeutic procedure in which the selected tissues are heated above normal physiological temperatures. It can be sought as an alternative cancer therapy that may have less side effects in contrast to radio or chemotherapy. Hyperthermia is usually carried out in two distinct temperature regimes³³⁻³⁶ (1) at high temperature, above 48°C for an irreversible treatment of cancer cells. The effect of temperature is drastic and non-reversible, highly efficient but risky due to collateral damages with a possibility of total ablation of tumor or tissue upon exceeding the vaporization temperature of water^{36,37} (2) A clinically relevant temperature ranging at $41-48^\circ\text{C}$ for hyperthermia treatment leads to

protein denaturation, cell function inactivation, oxidative stress, or rapid necrotic cell death³⁸. During therapy, cell apoptosis or thermal shock protein expression is induced. Tissue processes include changes in pH or perfusion and oxygenation of the tumor microenvironment. The effectiveness of the therapy mainly depends on the achieved temperature, time of exposure, and characteristics of the cancer cells³⁹

For the most advantageous feature of hyperthermia in neoplastic disease treatment compared with classic techniques like surgery, chemotherapy, and radiotherapy, hyperthermia tends to be less invasive but has to be combined with traditional methods in order to increase the overall efficacy. However, treatment towards recovery from cancer requires localized, controlled, and efficient heating. This important task can be fulfilled by designing and developing alternative techniques utilizing nanoparticle-based systems for non-contact heating.

For magnetothermal therapy by using magnetic nanoparticles, heating is realized by taking help of the magnetic properties of these magnetic nanoparticles. In general, the effect can be achieved by using an alternating magnetic field (AMF) on NPs, which eventually heats up inductively due to the following mechanisms originating from power loss under the AMF:

1. Hysteresis losses during the irreversible magnetization process. It can be estimated by taking into account the area of the



hysteresis loop, which works mostly for particles that are not in the superparamagnetic state. In superparamagnetic state, area inside magnetic hysteresis loop is zero and so there is no contribution of this mechanism in total particle heating. It is thus a characteristic for particles with a size above the superparamagnetic regime.

2. Eddy currents, which depend strongly on the electric conductivity of the material. Once the dielectric material is taken into account, this type of loss has a very low contribution (For eg ferrites')⁴⁰.
3. Residual losses identified specifically as Néel and Brownian relaxations, which are strongly dependent on particle size, shape, agglomeration, etc⁴¹.

When the particles are in a superparamagnetic state, i.e., they are below the certain critical particle size (for Fe₃O₄, approximately 30 nm)⁴² residual losses (Néel and Brownian relaxations) upon magnetization–demagnetization cycles⁵ are dominant in heat generation. The Néel relaxation mechanism refers to the rotating of the magnetic moments within each particle (inner particle relaxation), whereas Brownian relaxation is connected with rotation of the entire nanoparticle with the setting of magnetic moments in accordance with the field direction (outer particle relaxation)^{43,44}.

The magnetic nanoparticles (MNPs) are introduced into the cells by the process of endocytosis. The leaky vasculature of

cancerous tissue absorbs larger amounts of MNPs than those of normal tissue⁴⁵⁻⁴⁶. Moreover, the biomolecules such as antibodies can be easily attached to the MNPs. MNPs like iron oxides can also be used as a magnetic factor in multifunctional nano constructs for being used in diagnostic imaging capabilities and targeting drugs^{47,48}.

The main aim of the present study is to synthesize stable Fe₃O₄ NPs doped with Y³⁺ ions by using a fast and efficient single step process which will be suitable for magnetic hyperthermia treatment with one ultimate goal relying on investigations of cell viability after magnetic hyperthermia treatment on breast cancer 4T1 cells.

2. EXPERIMENTAL METHODS

2.1.Synthesis:

For synthesizing Fe₃O₄ NPs, we took 8 mmol of FeCl₃·6H₂O and 4 mmol of FeSO₄·7H₂O, dissolved them in water and sonicated them for 30 min. Then, 5 mL of NH₄OH (25%) was added at a rate of approximately 2 drops/min. The mixture was sonicated for 10 min and then centrifuged and washed twice with ethanol/water (1/4). We finally washed the product with water to remove ammonia residue if any.

The synthesis of Y³⁺ doped Fe₃O₄ NPs were carried out analogously to the synthesis of the Fe₃O₄ sample. The Y³⁺ ions were added to the starting materials with appropriate molar ratios of Y³⁺ calculated from the formula: Y³⁺_xFe²⁺₂Fe³⁺_{2-x}O₄. For 0.1% Y³⁺, 0.004 mmol



of $\text{YCl}_3 \cdot 6\text{H}_2\text{O}$ was added, for 1% Y^{3+} , 0.04 mmol of $\text{YCl}_3 \cdot 6\text{H}_2\text{O}$, for 10% Y^{3+} , 0.4 mmol of $\text{YCl}_3 \cdot 6\text{H}_2\text{O}$, and for 50% Y^{3+} , 2 mmol of $\text{YCl}_3 \cdot 6\text{H}_2\text{O}$ were added.

2.2 X-ray Diffraction (XRD), Transmission Electron Microscopy (TEM), and Scanning Electron Microscopy:

X-ray powder diffraction measurements of the $\text{Fe}_3\text{O}_4:\text{Y}$ samples were performed by Bruker AXE D8 diffractometer using $\text{Cu K}\alpha$ radiation, in the wide 2θ range. The samples' crystallographic properties were analyzed by Rietveld refinement with the help of the Fullprof 2k program (Rodriguez-Carvajal, J., 2016, FullProf, ver. 5.8).

The particle size and the morphology of the samples have been determined by SEM using a Zeiss Auriga Neon 40 microscope at an acceleration voltage of 5 kV.

HR TEM investigations have been conducted on an FEI Talos F200X transmission microscope at 200 kV. The measurements have been performed in TEM and STEM modes using high-angle annular dark field imaging (HAADF). An energy-dispersive X-ray spectroscopy (EDX) detector was used for mapping element distribution. The samples for the TEM observations were prepared by dropping the colloid particle dispersion on a carbon film supported on a 300 mesh copper grid.

2.3 Magnetic Characterization:

Magnetization measurements including saturation magnetization, zero-field cooling

(ZFC), and field cooling (FC) measurements were performed on a Quantum Design MPMS XL - 7 SQUID magnetometer. FC-ZFC measurements were collected in the range of 2.0 to 300 K at an applied magnetic field of 20 mT. Field dependent hysteresis loops of magnetisation (M-H) were measured at a temperature of 310 K with an applied field range from 0 to 5.0 T.

RESULT & DISCUSSION

3.1 Structural Characterization:

The crystal structure has been confirmed by the XRD measurement. The diffraction patterns for W1, Y1, Y2, and Y3 samples (Figure 1) are single-phase materials with a spinel structure (space group: $\text{Fd}\bar{3}\text{m}$). The lattice parameters of the samples were determined using the Rietveld method in the Supporting Information (Table S1). Obtained results are indicative of a non-stoichiometric character of the samples. The lattice parameters values are slightly increasing with increasing Y^{3+} concentration.

Table S1. The crystallographic model for $\text{Fe}_3\text{O}_4:\text{Y}$ nanoparticles.

Atom name	Atomic positions		
	x	y	z
Fe	0.125	0.125	0.125
Fe/Y	0.5	0.5	0.5
O	0.248(1)	0.248(1)	0.248(1)



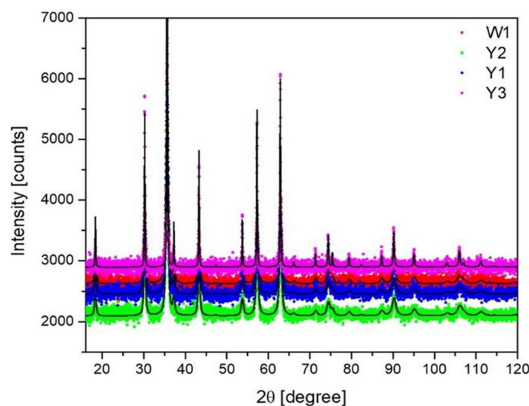


Figure 1. X-ray diffraction patterns of the Fe_3O_4 NPs as a function of Y^{3+} cation content.

The averaged dimensions of the nanocrystallites were assessed using the Scherrer method:

$$D = \frac{k\lambda}{\cos \Theta \sqrt{\beta^2 - \beta_0^2}} \quad (1)$$

where D is the grain size, β_0 is the apparatus broadening, β is the full width at half maximum, θ is the angle, k is a constant (usually equal to 0.9), and λ is the X-ray wavelength. The results of the Rietveld refinement together with crystallite sizes are gathered in Table 1.

Table 1. Lattice Parameter a and Nanoparticle Size Extracted from the XRD Data

sample	percent of Y^{3+}	lattice parameter [\AA]	crystallite size [nm]
W1	0%	8.3466(8)	14 ± 3
Y1	0.1%	8.3469(8)	13 ± 2
Y2	1%	8.3467(6)	14 ± 3
Y3	10%	8.3543(2)	56 ± 7

It is well known that the incorporation of the trivalent cations such as Nd^{3+} , Cr^{3+} , Y^{3+} , or In^{3+} into the structure of the magnetite strongly

affects magnetic, dielectric, and structural properties of the Fe_3O_4 NPs. Rare-earth cations such as La^{3+} , Sm^{3+} , or Dy^{3+} , by substituting Fe^{3+} in octahedral position, can force the Fe^{3+} ion for preferential occupation of the tetrahedral crystallographic site. This is expected to ease the crystal lattice tension, and therefore the density of the Fe^{3+} ions will increase the permeability, and as a logical consequence, the resistance of NPs will increase²⁵⁻²⁷. In this work, the intention of using Y^{3+} cations as a dopant was to increase the magnetization of the magnetite. The comparison of the literature data suggests that Y^{3+} will preferentially enter the octahedral sites and, as a result of radius incompatibility (ionic radii: Y^{3+} at eightfold coordination, 1.019 \AA and Fe^{3+} at eightfold coordination, 0.78 \AA), the cell volume will expand, and therefore the cell parameter has to increase accordingly²⁷. Actually, this trend is consistent with the Rietveld refinement until maximum Y^{3+} concentration is achieved (10 mol %) at the Fe^{3+} octahedral site. This phenomenon (together with charge incompatibility) has to be always taken into account at the stage of the given material synthesis planning.

The sample morphology and particle size of the Fe_3O_4 NPs doped by the Y^{3+} ions were characterized by using SEM techniques (Figure 2). The normal distribution was fitted to the size distribution histograms obtained from the analysis of SEM images. The size



and particle distribution (standard deviation (SD)) were calculated and are presented in Table 2.

As one can see, the W1, Y1, and Y2 materials are composed of polydispersed NPs with SDs of approximately 3–4 nm.

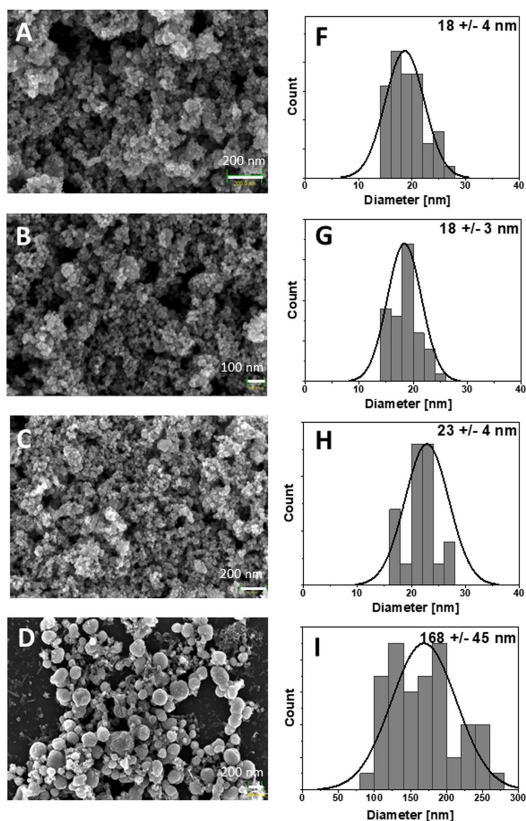


Figure 2. SEM images and histograms of Fe₃O₄ NPs doped by Y³⁺ ions. (A, F) Fe₃O₄ (W1), (B, G) 0.1% Y³⁺-doped Fe₃O₄ (Y1), (C, H) 1% Y³⁺-doped Fe₃O₄ (Y2), and (D, I) 10% Y³⁺-doped Fe₃O₄ (Y3) MNPs.

Table 2. Diameter and Standard Deviation (SD) of the MNPs

sample	diameter [nm]	SD
W1	18	4
Y1	18	3
Y2	23	4
Y3	168	45

It can be noticed that the particle size of the Y1–Y3 magnetite samples doped with yttrium ions increases upon the increase of the Y³⁺ cation content. The mean particle size of the Y3 sample is approximately 170 nm with an SD of 45 nm. This behavior might point out two things: either fast particle growth, which might be promoted by the increased Y³⁺ amount, or the formation of one or several thermodynamically more favored and stable unknown amorphous phases, which can be more convincingly related. The SEM results clearly indicate particle agglomeration, which is in accordance with the TEM results (Figure 3).

Elemental analysis and mapping of the Fe₃O₄ NP compositions was conducted by means of EDX spectroscopy connected with TEM microscopy in order to confirm the crucial ratio between elements (Table 3). As it can be seen, the ratios between iron and oxygen ions are in a good correspondence with theoretical values. The same has been observed in the case of Y³⁺ doping. The results of element mapping are shown in Figure 3. Elemental colocalizations of Fe, Y, and O elements were found indicating the homogenous distribution of all elements within Fe₃O₄ NPs.



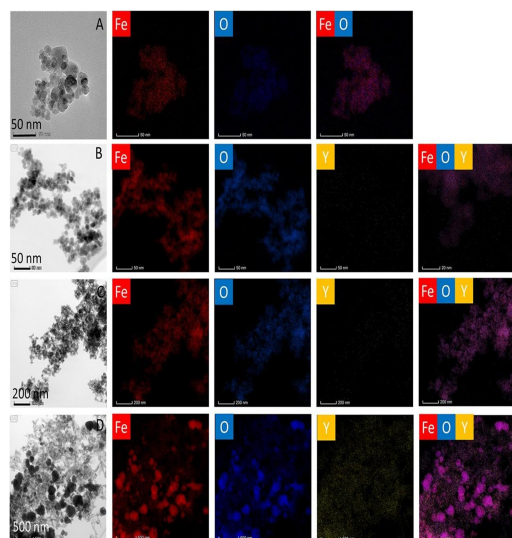


Figure 3. TEM and EDX mapping of Fe_3O_4 NPs doped by Y^{3+} ions. (A) Fe_3O_4 (W1), (B) 0.1% Y^{3+} -doped Fe_3O_4 (Y1), (C) 1% Y^{3+} -doped Fe_3O_4 (Y2), and (D) 10% Y^{3+} -doped Fe_3O_4 (Y3) MNPs.

Table 3. Elemental Analysis of EDX of Fe_3O_4 NPs Doped with Yttrium Ions

sample	$2\text{Fe}^{3+}/\text{Fe}^{2+}/\text{O}^{2-}$ (%)		$\text{Y}^{3+}/2\text{Fe}^{3+}\text{Fe}^{2+}$ (%)	
	theoretical value	experimental value	theoretical value	experimental value
W1	75.0	55.2 ± 9.4		
Y1	75.0	53.0 ± 9.1	0.10	0.20 ± 0.02
Y2	74.5	53.4 ± 9.0	0.70	0.70 ± 0.06
Y3	70.3	52.0 ± 9.0	6.80	7.30 ± 0.70

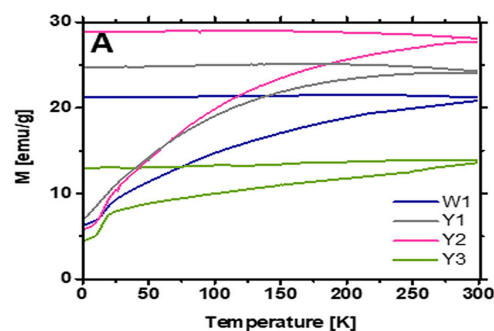
3.2. Magnetic Properties:

In order to determine the blocking temperature for the samples, the ZFC/FC measurements were performed. After exceeding this temperature, the system becomes superparamagnetic. The ZFC/FC measurements consist of cooling the sample without a magnetic field, then slowly heating it in the magnetic field and cooling it again in the same field. The relation between magnetization and temperature was measured

(Figure 4A) in the temperature range from 2.0 to 300.0 K in an external magnetic field of 20.0 mT. The blocking temperature was not determined because the samples in the entire temperature range exhibited ferromagnetic properties. This is illustrated by the gap (hysteresis) between the two ZFC/FC graph curves (Figure 4A).

The ferromagnetic properties of the samples were confirmed by the measurement of magnetization (M) as a function of the external magnetic field (B) (Figure 4B,C). The highest magnetization was obtained for the Y2 sample doped with 1 mol % yttrium (75 emu/g). Both samples Y1 and Y2 achieved higher magnetization than that of the sample without Y^{3+} ions, W1. The saturation magnetization of the samples decreased with the higher concentration of Y^{3+} ions.

Standard error propagation was estimated for SQUID measurements. The accuracy of mass measurement was $\Delta m = 10^{-4}$ g, and the accuracy of magnetic moment measurement was $\Delta \mu = 10^{-8}$ emu. The standard deviation of six measurements of $M(B)$ (made at the same temperature) was $\sigma_M = 1$ emu/g. An error account was made using eq 2. The estimated maximal



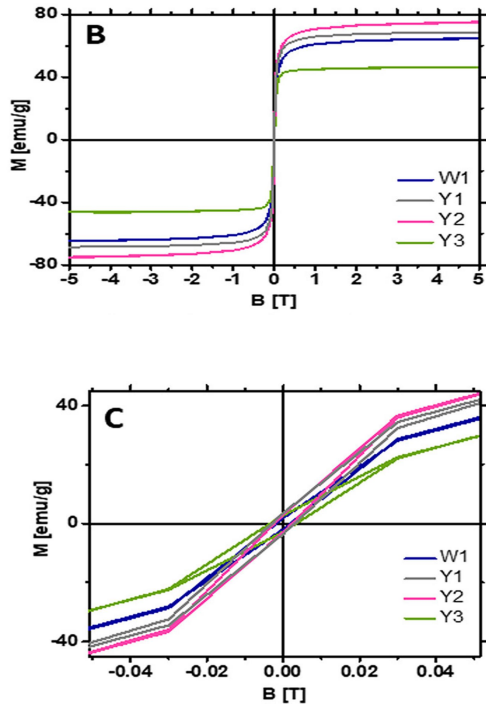


Figure 4. (A) ZFC/FC plot of W1 and Y1–Y3 samples. (B) Hysteresis loops at 310 K. (C) Zoom of the hysteresis loops at 310 K.

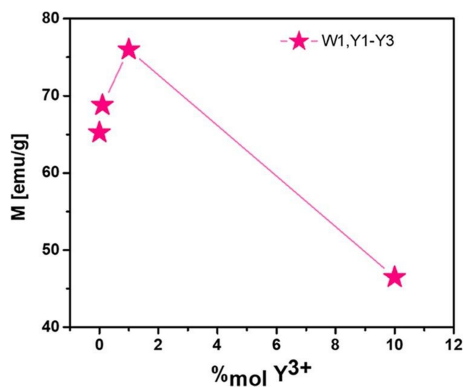


Figure 5. Graph of dependence of magnetization on % yttrium doping. Points are connected by a line to show the trend.

measurement uncertainty d_M of the magnetization depending on the magnetic field was 2.5 emu/g.

$$d_M = \sqrt{\frac{1}{3} \left(\frac{\Delta \mu}{m} \right)^2 + (\sigma_M)^2 + \frac{\langle \mu \rangle^2 \Delta_m^2}{3 m^4}} \quad (2)$$

where m is the sample mass and $\langle \mu \rangle$ is the magnetic moment. The dependence of samples' saturation magnetization on the concentration of yttrium ions is shown in Figure 5. The maximum magnetization is achieved by the sample Y1 (1% of Y³⁺), which confirms that the magnetization increases with the doping concentrations to reach the maximum. Then, the magnetization decreases with a further increase of the percentage of doping. The magnetization of ferrites comes from the difference in the over intra sublattice A–A and B–B interactions (Neél model). Therefore, the saturation of magnetization comes from the sum of vectors of the net magnetic moments of the individual A and B sublattices. The magnetization directly shows the distribution of the Fe³⁺ ions between the two sublattices. If the Fe³⁺ ions occupy both octahedral and tetrahedral sites, the ferrimagnetic ordering will be observed. It is known that the magnetization is higher in MNPs than in bulk materials because of the formation of a partially inversed spinel. The location of Fe³⁺ ions on tetrahedral sites causes Fe³⁺A–O–Fe³⁺B super- exchange interactions and the increase of magnetization is observed.



By substituting Fe^{3+} ions by non-magnetic Y^{3+} ions, the magnetization of the octahedral coordination should be reduced, resulting in a decrease in magnetization. However, with a small amount of Y^{3+} addition (up to 1%), the trend is opposite. In the case of small Y^{3+} concentrations, the magnetization increases. There are two possible explanations of the observed effect: first, if non-magnetic Y^{3+} ions at low concentrations enter spinel tetrahedral sites, leaving Fe^{3+} in octahedral sites, this can also lead to an increase of magnetization. However, the literature data suggests that Y^{3+} should prefer the octahedral sites. Second, the presence of Y^{3+} ions increases the size of nanoparticles, which increases blocking temperature and saturation magnetization for low dopant concentrations. Although further increasing Y^{3+} doping keeps increasing the size of the MNPs, finally, this leads to the decrease of saturation magnetization because non-magnetic yttrium replaces magnetic iron in octahedral sites.

CONCLUSION

Single phase Y^{3+} doped Fe_3O_4 Nanoparticles have been synthesized with different amounts of doping of Y^{3+} ions. The mean particle size of Y^{3+} samples is approximately 70 nm. EDX spectroscopy and TEM microscopy confirm the ratio between iron and oxygen ions in good correspondence with the theoretical values. The highest magnetisation of 75 emu/g has been obtained for 1% Yttrium doped sample.

ACKNOWLEDGEMENT

I highly appreciate the support of UGC-DAE Consortium for Scientific Research, Indore for providing the characterisation facilities like SQUID-VSM, TEM, SEM etc. The technical support of Kumar Ashay and Kshitij Kashyap is also appreciated.

REFERENCES:

- (1) Bate, G. Magnetic Oxides Part 2; Craik, D. J. John Wiley & Sons: New York, 1975, pp 705.
- (2) Arruebo, M.; Fernández-pacheco, R.; Ibarra, M. R.; Santamaría, J. Magnetic nanoparticles for drug delivery. *Nano Today* 2007, 2, 22–32.
- (3) Pradhan, P.; Giri, J.; Samanta, G.; Sarma, H. D.; Mishra, K. P.; Bellare, J.; Banerjee, R.; Bahadur, D. Comparative evaluation of heating ability and biocompatibility of different ferrite-based magnetic fluids for hyperthermia application. *J. Biomed. Mater. Res. B. Appl. Biomater.* 2007, 81B, 12–22.
- (4) Huff, T. B.; Tong, L.; Zhao, Y.; Hansen, M. N.; Cheng, J. X.; Wei, A. Hyperthermic effects of gold nanorods on tumor cells. *Nanomedicine* 2007, 2, 125–132.
- (5) Kim, D. H.; Nikles, D. E.; Brazel, C. S. Synthesis and characterization of multifunctional chitosan- MnFe_2O_4 nanoparticles for magnetic hyperthermia and drug delivery. *Materials* 2010, 3, 4051–4065.



- (6) Kim, D. H.; Nikles, D. E.; Johnson, D. T.; Brazel, C. S. Heat generation of aqueously dispersed CoFe₂O₄ nanoparticles as heating agents for magnetically activated drug delivery and hyperthermia. *J. Magn. Magn. Mater.* 2008, 320, 2390–2396.
- (7) Na, H. B.; Song, I. C.; Hyeon, T. Inorganic nanoparticles for MRI contrast agents. *Adv. Mater.* 2009, 21, 2133–2148.
- (8) van Landeghem, F. K. H.; Maier-Hauff, K.; Jordan, A.; Hoffmann, K.-T.; Gneveckow, U.; Scholz, R.; Thiesen, B.; Brück, W.; von Deimling, A. Post-mortem studies in glioblastoma patients treated with thermotherapy using magnetic nanoparticles. *Biomaterials* 2009, 30, 52–57.
- (9) Schulz, M. J.; Shanov, V. N.; Yun, Y. Nanomedicine design of particles, sensors, motors, implants, robots, and devices; Artech House: MA, USA 2009, p.549.
- (10) Thapa, D.; Palkar, V. R.; Kurup, M. B.; Malik, S. K. Properties of magnetite nanoparticles synthesized through a novel chemical route. *Mater. Lett.* 2004, 58, 2692–2694.
- (11) Lee, J. H.; Huh, Y. M.; Jun, Y.; Seo, J.; Jang, J.; Song, H. T.; Kim, S.; Cho, E. J.; Yoon, H. G.; Suh, J. S.; et al. Artificially engineered magnetic nanoparticles for ultra-sensitive molecular imaging. *Nat. Med.* 2007, 13, 95–99.
- (12) Mendoza-Garcia, A.; Sun, S. Recent advances in the high- temperature chemical synthesis of magnetic nanoparticles. *Adv. Funct. Mater.* 2016, 26, 3809–3817.
- (13) Wu, L.; Mendoza-Garcia, A.; Li, Q.; Sun, S. Organic phase syntheses of magnetic nanoparticles and their applications. *Chem. Rev.* 2016, 116, 10473–10512.
- (14) Zhao, Z.; Chi, X.; Yang, L.; Yang, R.; Ren, B. W.; Zhu, X.; Zhang, P.; Gao, J. Cation exchange of anisotropic-shaped magnetite nano-particles generates high-relaxivity contrast agents for liver tumor imaging. *Chem. Mater.* 2016, 28, 3497–3506.
- (15) Szczerba, W.; Żukrowski, J.; Przybylski, M.; Sikora, M.; Safonova, O.; Shmeliov, A.; Nicolosi, V.; Schneider, M.; Granath, T.; Oppmann, M.; et al. Pushing up the magnetisation values for iron oxide nanoparticles via zinc doping: X-ray studies on the particle's sub- nano structure of different synthesis routes. *Phys. Chem. Chem. Phys.* 2016, 18, 25221–25229.
- (16) Bram, S.; Gordon, M. N.; Carbonell, M. A.; Pink, M.; Stein, B. D.; Morgan, D. G.; Aguila, D.; Aromi, G.; Skrabalak, S. E.; Losovyj, Y.; et al. Zn²⁺ ion surface enrichment in doped iron oxide nanoparticles leads to charge carrier density enhancement. *ACS Omega* 2018, 3, 16328–16337.
- (17) Liang, X.; Wang, X.; Zhuang, J.; Chen, Y.; Wang, D.; Li, Y. Synthesis of nearly monodisperse iron oxide and oxyhydroxide nanocrystals. *Adv. Funct. Mater.* 2006, 16, 1805–1813.



- (18) Colognato, R.; Bonelli, A.; Bonacchi, D.; Baldi, G.; Migliore, L. Analysis of cobalt ferrite nanoparticles induced genotoxicity on human peripheral lymphocytes: comparison of size and organic grafting- dependent effects. *Nanotoxicology* 2007, 1, 301–308.
- (19) Pacchierotti, F.; Bellusci, M.; La Barbera, A.; Padella, F.; Mancuso, M.; Pasquo, A.; Grollino, M. G.; Leter, G.; Nardi, E.; Cremisini, C.; Giardullo, P. Biodistribution and acute toxicity of a nanofluid containing manganese iron oxide nanoparticles produced by a mechanochemical process. *Int. J. Nanomed.* 2014, 9, 1919–1929.
- (20) Asmatulu, R.; Garikapati, A.; Misak, H. E.; Song, Z.; Yang, S.-Y.; Wooley, P. Cytotoxicity of magnetic nanocomposite spheres for magnetic resonance imaging, cell labeling, and cell sorting agents. *Bioconjugate and organic materials*; Stanislaw Grundas, IntechOpen, 2011, 483–502.
- (24) De Silva, C. R.; Smith, S.; Shim, I.; Pyun, J.; Gutu, T.; Jiao, J.; Zheng, Z. Lanthanide(III)-doped magnetite nanoparticles. *J. Am. Chem. Soc.* 2009, 131, 6336–6337.
- (25) Milanovic, M.; Moshopoulou, E. G.; Stamopoulos, D.; Devlin, E.; Giannakopoulos, K. P.; Kontos, A. G.; Eleftheriadis, K.; Gini, M. I.; Nikolic, L. M. Structure and magnetic properties of $Zn_{1-x}In_xFe_2O_4$ and $Zn_{1-x}Y_xFe_2O_4$ nanoparticles prepared by coprecipitation. *Ceram. Int.* 2013, 39, 3235–3242.
- (26) Verma, S.; Chand, J.; Singh, M. Effect of In^{3+} ions doping on the structural and magnetic properties of $Mg_{0.2}Mn_{0.5}Ni_{0.3}In_xFe_2O_4$ spinel ferrites. *J. Magn. Magn. Mater.* 2012, 324, 3252–3260.
- (27) Ishaque, M.; Islam, M. U.; Khan, M. A.; Rahman, I. Z.; Genson, A.; Hampshire, S. Structural, electrical and dielectric properties of yttrium substituted nickel ferrites. *Phys. Rev. B: Condens. Matter* 2010, 82, 1532–1540.
- (28) Shinde, T. J.; Gadkari, A. B.; Vasambekar, P. N. Effect of Nd^{3+} substitution on structural and electrical properties of nanocrystalline generating SiO_2 -coated
- (21) Jang, J.-t.; Nah, H.; Lee, J.-H.; Moon, S. H.; Kim, M. G.; Cheon, J. Critical enhancements of MRI contrast and hyperthermic effects by dopant-controlled magnetic nanoparticles. *Angew. Chem., Int. Ed.* 2009, 48, 1234–1238.
- (22) Zhu, S.; Xu, X.; Rong, R.; Li, B.; Wang, X. Evaluation of zinc-doped magnetite nanoparticle toxicity in the liver and kidney of mice after sub-chronic intragastric administration. *Toxicol. Res.* 2016, 5, 97–106.
- (23) Groman, E. V.; Bouchard, J. C.; Reinhardt, C. P.; Vaccaro, D. E. Ultrasmall mixed ferrite colloids as multidimensional



- lanthanide-doped NaYF₄ Adv. 2017, 7, 30262–30273.
- (29) Xing, Q.; Peng, Z.; Wang, C.; Fu, Z.; Fu, X. Doping effect of Y³⁺ ions on the microstructural and electromagnetic properties of Mn–Zn ferrites. Phys. B 2012, 407, 388–392.
- (30) Shirsath, S. E.; Toksha, B. G.; Jadhav, K. M. Structural and magnetic properties of In³⁺ substituted NiFe₂O₄. Mater. Chem. Phys. 2009, 117, 163–168.
- (31) Cvejić, Z.; Rakić, S.; Jankov, S.; Skuban, S.; Kapor, A. Dielectric properties and conductivity of zinc ferrite and zinc ferrite doped with yttrium. J. Alloys Compd. 2009, 480, 241–245.
- (32) Hashim, M.; Alimuddin; Kumar, S.; Shirsath, S. E.; Kotnala, R. K.; Chung, H.; Kumar, R. Structural properties and magnetic interactions in Ni_{0.5}Mg_{0.5}Fe₂–XCrXO₄ (0 ≤ X ≤ 1) ferrite nanoparticles. Powder Technol. 2012, 229, 37–44.
- (33) Yonezawa, M.; Otsuka, T.; Matsui, N.; Tsuji, H.; Kato, K. H.; Moriyama, A.; Kato, T. Hyperthermia induces apoptosis in malignant fibrous histiocytoma cells in vitro. Int. J. Cancer 1996, 66, 347–351.
- (34) Sellins, K. S.; Cohen, J. J. Hyperthermia induces apoptosis in thymocytes. Radiat. Res. 1991, 126, 88–95.
- (35) Christophi, C.; Winkworth, A.; Muralidharan, V.; Evans, P. The treatment of malignancy by hyperthermia. Surg. Oncol. 1998, 7, 83.
- (36) Welch, A. J.; Motamedi, M.; Rastegar, S.; LeCarpentier, G. L.; Jansen, D. Laser thermal ablation. Photochem. Photobiol. 1991, 53, 815–823.
- (37) Goldstein, L. S.; Dewhirst, M. W.; Repacholi, M.; Kheifets, L. Summary, conclusions and recommendations: adverse temperature levels in the human body. Int. J. Hyperthermia 2009, 19, 373–384.
- (38) Jaque, D.; Maestro, L. M.; del Rosal, B.; Haro-Gonzalez, P.; Benayas, A.; Plaza, J. L.; Rodríguez, E. M.; Solé, J. G. Nanoparticles for photothermal therapies. Nanoscale 2014, 6, 9494–9530.
- (39) Raaphorst, G. P.; Freeman, M. L.; Dewey, W. C. Radiosensitivity and recovery from radiation damage in cultured CHO cells exposed to hyperthermia at 42.5 or 45.5 degrees C. Radiat. Res. 1979, 79, 390–402.
- (40) Dutz, S.; Hergt, R. Magnetic particle hyperthermia a promising tumour therapy? Nanotechnology 2014, 25, 452001.
- (41) Zhang, Y.; Zhai, Y. Magnetic induction heating of nano-sized ferrite particle. In advances in induction and microwave heating of mineral possible drug delivery systems. ASME Int. Mech. Eng. Congr. Expo. 2012, 10, 911–918.
- (42) Dunlop, D. J. Superparamagnetic and single-domain threshold sizes in magnetite. J. Geophys. Res. 1973, 78, 1780–1793.



(43) Carrey, J.; Mehdaoui, B.; Respaud, M. Simple models for dynamic hysteresis loop calculations of magnetic single-domain nanoparticles: Application to magnetic hyperthermia optimization. *J. Appl. Phys.* 2011, 109, No. 083921.

(44) Dutz, S.; Hergt, R. Magnetic nanoparticle heating and heat transfer on a microscale: Basic principles, realities and physical limitations of hyperthermia for tumour therapy. *Int. J. Hyperthermia* 2013, 29, 790–800.

(45) Jordan, A.; Scholz, R.; Wust, P.; Schirra, H.; Schiestel, T.; Schmidt, H.; Felix, R. Endocytosis of dextran and silan-coated Chem. 2007, 18, 1763–1771.

(46) Jordan, A.; Scholz, R.; Wust, P.; Föhling, H.; Felix, R. Magnetic fluid hyperthermia (MFH): Cancer treatment with AC magnetic field induced excitation of biocompatible superparamagnetic nanoparticles. *J. Magn. Magn. Mater.* 1999, 201, 413–419.

(47) Nasongkla, N.; Bey, E.; Ren, J.; Ai, H.; Khemtong, C.; Guthi, J. S.; Chin, S. F.; Sherry, A. D.; Boothman, D. A.; Gao, J. Multifunctional polymeric micelles as cancer-targeted, MRI-ultrasensitive drug delivery systems. *Nano Lett.* 2006, 6, 2427–2430.

(48) Mornet, S.; Vasseur, S.; Grasset, F.; Duguet, E. Magnetic nanoparticle design for medical diagnosis and therapy. *J. Mater. Chem.* 2004, 14, 2161–2175.

